Inferring activity from fluid flow in continuum models of active matter

Aditya Mohapatra,* Sagarika Adhikary,† and Rajesh Singh‡
Department of Physics, Indian Institute of Technology Madras, Chennai, India

Active matter systems are driven out of thermodynamic equilibrium by localized, microscale energy dissipation. While hydrodynamic continuum frameworks are highly successful at simulating these non-equilibrium phenomena (the forward problem), characterizing real-world active materials is fundamentally bottle-necked by the difficulty of measuring active stresses directly. This paper addresses the inverse problem using deep learning: model inference and model selection from observable flow field data of active fluids. We formulate a generalized hydrodynamic inversion framework applied to two cornerstone paradigms of active continuum physics: Active Model H (representing scalar active matter) and Active Nematics (representing active systems with orientational order). We demonstrate that the kinetic energy spectrum obtained from the fluid flow fields preserve a high-fidelity signature of activity to infer parameters of active model H and active nematics. Our deep learning method presents a principled way to bear upon questions of model inference and selection given the flow field data in continuum models of active matter.

arXiv:2607.20100v1 [cond-mat.soft] 22 Jul 2026

I. INTRODUCTION

Active matter defines a fascinating class of non-equilibrium systems composed of individual constituents that consume internal or environmental energy to generate spectacular emergent phenomena. [1–4]. Continuum theories of active matter are written in terms of hydrodynamic variables such as density $\rho(\mathbf{r}, t)$, velocity $\mathbf{v}(\mathbf{r}, t)$, and orientation $\mathbf{n}(\mathbf{r}, t)$. The frameworks of continuum fields successfully capture the large-scale physics of active fluids [3–6]. In traditional theoretical modeling (the forward problem), known activity parameter within an active stress tensor to predict how the fluid will flow [5, 6]. Depending on the sign of parameter, the active units act as contractile (puller) or extensile (pusher). This forward approach is highly effective for simulating idealized systems. However, when confronting real-world biological systems or complex synthetic microswimmers, a major bottleneck arises: activity is difficult to measure directly. This work addresses the inverse problem: Can we look at the fluid flow and deduce the underlying activity responsible for the flow? For active systems at the microscale, the fluid flow operate at a low Reynolds number, the surrounding fluid acts as an instantaneous transmitter of force densities, governed by the Stokes equation. Because the flow field $\mathbf{v}(\mathbf{r})$ is directly coupled to the active stress through the Stokes equation, the fluid flow itself preserves a high-fidelity spatial map of the system's underlying activity. Inference of active nematics using machine learning framework has received considerable attention recently [7–13], while systematic inference method of scalar field theories of active matter [14, 15] remains unexplored. In this paper, we present a machine learning framework which can be simultaneously applied to scalar theories of active matter as well active nematics.

* adityamohapatra217@gmail.com
† a.sagarika@physics.iitm.ac.in
‡ rsingh@physics.iitm.ac.in

By framing the extraction of active properties as a problem of hydrodynamic inference, this paper explores the theoretical and computational frameworks required to reconstruct activity parameters solely from observable flowfield data. To this end, we utilize deep learning and active field theory to infer model parameters and select between models using flow field data. First, in Sec. II, we present our theoretical framework for continuum descriptions of active matter. This is the forward problem: obtaining fluid flow given activity in distinct models of active matter. Second, in Sec. III, we show how machine learning framework can be deployed to infer parameters of model systems from the measured flow field. In particular, we show that the energy spectrum retains high-fidelity signature of activity which can be used for both model inference and model selection. Third, in Sec. IV, we present details of the model selection procedure with-ing our ML framework. Finally, in Sec V, we summarize our results and present future directions. Overall, our results present a principled framework for model inference and model selection from flow field data in continuum models of active matter.

II. MODELS OF ACTIVE FLUIDS

In this section, we present the forward problem of computing flow field given a continuum model of active matter. We consider two workhorses of continuum models of active matter with hydrodynamic interactions. At the continuum level, the dynamics of active matter systems is given in terms of active field theories [16]. For systems without no global polar, a continuum theory can be given in terms of a scalar order parameter. Such a theory with mass and momentum conservation is referred to as active model H in literature [14, 15]. In presence of nematic order in the system, the dynamics of the systems is given terms of the well-known models refereed to as active nematics [3, 6, 17, 18]. We describe both these models in detail below.

A. Active model H

Active Model H is used to describe the hydrodynamic behavior of scalar active matter, such as self-propelled microswimmers suspended in a momentum-conserving solvent without explicit orientational alignment. The nomenclature of active model H follows from the Hohenberg-Halperin classification [19]. While the traditional, passive Model H couples the diffusion of a conserved scalar field (like particle concentration) to a fluid velocity field, its active counterpart injects non-equilibrium physics by introducing an intrinsic active stress tensor that breaks time-reversal symmetry. For contractile active particles, this microscale driving force functions effectively as a negative interfacial tension, causing fluid flow to spontaneously stretch phase interfaces [14, 15]. Spontaneous stretching of interfaces for contractile active stress in active model H leads to a self-shearing instability [15]. The result is a dynamical steady-state of active fluids maintained by the competing Ostwald ripening and self-sharing instability. The dynamical steady-state of active model H for contractile activity has also been refereed to as scalar active turbulence in the literature [20, 21]. In this section, we present the forward problem to simulate active model H for a prescribed activity.

We now present the equations describing the dynamics. Consider a conserved scalar field $\phi(\mathbf{r},t)$ in a momentum-conserving fluid of velocity $\mathbf{v}(\mathbf{r},t)$. The dynamics of the the scalar field is then given in terms of contributions to the flux from mechanical sector ($\mathbf{v}\phi$) and diffusive sector as described below. The explicit form is:

$$\frac{\partial \phi}{\partial t} + \boldsymbol{\nabla}\cdot\left(\phi\mathbf{v} - \boldsymbol{\nabla}\frac{\delta\mathcal{F}}{\delta\phi}\right) = 0, \tag{1a}$$

$$\mathcal{F}[\phi] = \int\left(-\frac{b}{2}\phi^2 + \frac{b}{4}\phi^4 + \frac{\kappa_p}{2}(\nabla\phi)^2\right)d\mathbf{r}. \tag{1b}$$

Here, $\mathcal{F}$ is the Landau-Ginzburg free energy functional.

The fluid flow, in the limit of low Reynolds number (as applicable to microswimmers), is obtained from the solution of the Stokes equation:

$$\boldsymbol{\nabla}\cdot\boldsymbol{\sigma} = -\boldsymbol{\nabla}\cdot(\boldsymbol{\Sigma}^{\mathrm{A}} + \boldsymbol{\Sigma}^{\mathrm{E}}). \tag{2}$$

Here $\boldsymbol{\sigma}$ is the Cauchy stress tensor, which is given as:

$$\sigma_{ij} = -p\delta_{ij} + \eta(\nabla_i v_j + \nabla_j v_i) \tag{3}$$

η is viscosity, $\mathbf{I}$ is the identity tensor, and p is the pressure field which contains all isotropic terms and ensures incompressibility ($\nabla\cdot\mathbf{v} = 0$) [22]. The deviatoric stresses $\boldsymbol{\Sigma}^{\mathrm{E}}$ and $\boldsymbol{\Sigma}^{\mathrm{A}}$ are then, in d-dimensions, given to the required order as:

$$\boldsymbol{\Sigma}^{\mathrm{E}} = -\kappa_p\mathbf{S}, \qquad \boldsymbol{\Sigma}^{\mathrm{A}} = -(\tilde{\kappa} - \kappa_p)\mathbf{S} = -\alpha\mathbf{S}, \tag{4}$$

$$\mathbf{S} \equiv (\nabla\phi)(\nabla\phi) - \tfrac{1}{d}|\nabla\phi|^2\mathbf{I}. \tag{5}$$

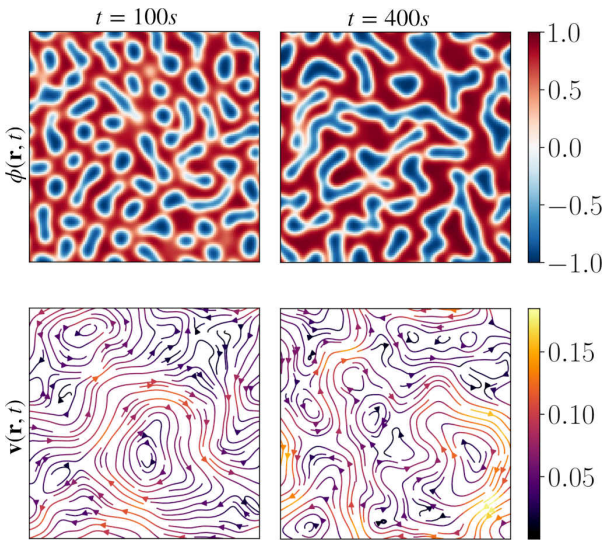

FIG. 1. **Active Model H**. Snapshots from simulation of Active Model H for the order-parameter field $\phi(\mathbf{r},t)$ (top row) and the induced velocity field $\mathbf{v}(\mathbf{r},t)$ (bottom row) at $t = 100$s, and 400s for $\kappa_p = 1.0$, $\tilde{\kappa} = -0.5$, $b = 0.5$. Colour in the top row maps $\phi \in [-1, 1]$; streamlines in the bottom row are coloured by the local speed $|\mathbf{v}|$.

It is worthwhile to note that the mechanical stress in the above equations $\boldsymbol{\Sigma}^A + \boldsymbol{\Sigma}^E = -\tilde{\kappa}\boldsymbol{S}$ is not derived from a free energy. Thus, in general, it breaks detailed balance. The coefficient α can be either positive (for extensile microswimmers) or negative (for contractile microswimmers) [5, 14, 15] unlike equilibrium systems where $\kappa > 0$ and the limit $\boldsymbol{\Sigma}^A = 0$ holds. In appendix A, we explain present our numerical method to solve the above equations. In Fig.1, we show two snapshots from steady-state of active model H for the order parameter as well as the corresponding velocity field.

B. Minimal Description of Active Nematics

Active Nematics [3, 6, 18, 23–26] extend the classical continuum hydrodynamics of passive nematic liquid crystals frameworks to systems of elongated, self-propelled units that exhibit long-range orientational alignment. While passive nematics relax toward uniform alignment to minimize elastic free energy, active nematics are driven far from equilibrium by localized, dipolar forces generated along the long axis of each constituent, such as crawling spindle-shaped cells or kinesin-driven microtubule bundles. This intrinsic active stress renders the uniformly aligned state inherently unstable, triggering a hydrodynamic instability that continuously disrupts the orientational order. Active nematic systems are modeled within a continuum hydrodynamic framework in which the coarse-grained velocity field $\mathbf{v}(\mathbf{r},t)$ is coupled to the nematic order parameter tensor $Q_{ij}(\mathbf{r},t)$ [3, 18].

As described in the previous section of active model

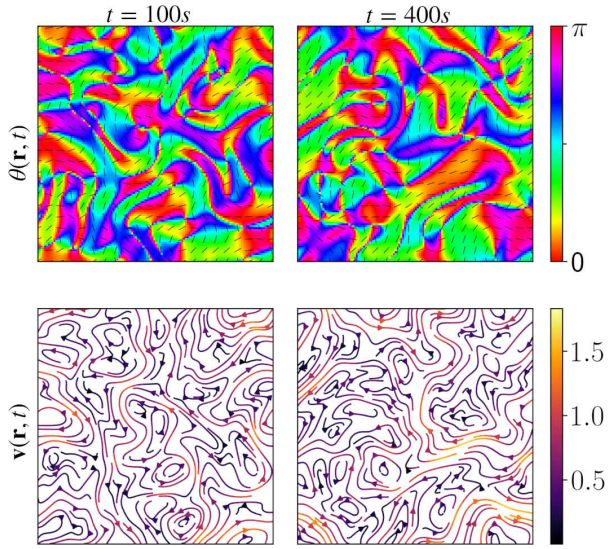

FIG. 2. **Active Nematics**. Snapshots of the nematic director field $\theta(\mathbf{r}, t)$ (top row) and the induced velocity field $\mathbf{v}(\mathbf{r}, t)$ (bottom row) at two time instances ($t = 100$s, and 200s) for $K = 1.0$, $\zeta = -0.5$. Colour in the top row maps the director field $\theta \in [0, \pi]$; streamlines in the bottom row are colored by the local speed $|\mathbf{v}|$.

H, the fluid flow is given by the Stokes equation. The incompressibility condition enforces $\nabla \cdot \mathbf{v} = 0$. For the case of active nematics, the fluid flow is driven by active stress $\Sigma^{\rm AN}_{ij}$:

$$\nabla_i \sigma_{ij} + \nabla_i \Sigma^{\rm AN}_{ij} = 0 \tag{6}$$

The Cauchy stress σ_{ij} was defined in Eq.(3). The active stress $\Sigma^{\rm AN}_{ij}$ for AN (active nematics) is:

$$\Sigma^{\rm AN}_{ij} = -\zeta Q_{ij}, \tag{7}$$

where ζ is the activity parameter (positive for extensile and negative for contractile systems). In this paper, we only consider contractile systems for simplicity. The nematic order parameter is expressed in terms of the director field $\mathbf{n} = (\cos\theta, \sin\theta)$ as

$$Q_{ij} = \left(n_i n_j - \tfrac{1}{d}\delta_{ij}\right). \tag{8}$$

Here, d is the spatial dimension. For two-dimensional systems ($d = 2$), a minimal description of active nematics can be formulated in terms of the coarse-grained director angle field $\theta(\mathbf{r}, t)$, where the nematic director is $\mathbf{n} = (\cos\theta, \sin\theta)$. The dynamics of θ is governed by [24]:

$$\partial_t \theta + \mathbf{v} \cdot \nabla\theta = K\nabla^2\theta + (\partial_x v_y - \partial_y v_x) \tag{9}$$

Here, K is the Frank elastic constant, while the Frank free energy is [24, 27]:

$$F_n = \frac{K}{2}\int |\boldsymbol{\nabla}\theta|^2 d\mathbf{r} \tag{10}$$

Together, Eq.(7) and Eq.(9) present a minimal hydrodynamic theory of active nematic fluids [24]. We have used these equations to generate data for inference framework described below. In Fig.2, we show two snapshots from steady-state of active nematic for the order parameter as well as the corresponding velocity field.

C. Kinetic Energy spectrum

To develop the machine learning framework, as we describe below, we analyze the spectra of the kinetic energy $E(k)$. The shell-averaged kinetic energy spectrum $E(k)$ is defined as

$$E(k,t) \equiv \frac{1}{n(k)} \sum_{k \le k' < k+\Delta k} \frac{1}{2}\left|\hat{\mathbf{v}}(\boldsymbol{k}', t)\right|^2 \tag{11}$$

Here $\hat{\mathbf{v}}(\boldsymbol{k}', t)$ is the discrete Fourier transform of the velocity field $\mathbf{v}$, and $n(k)$ is the number of discrete wavevectors $\boldsymbol{k}'$ satisfying $k \le |\boldsymbol{k}'| < k + \Delta k$. See appendix A for details. The summation condition below the sigma symbol: $k \le k' < k + 1$ means taking a spherical shell of radius k and thickness Δk, and the pre-factor $1/n(k)$ averages the kinetic energy over every wavenumber vector whose magnitude $k' = |\boldsymbol{k}'|$ falls inside that specific shell. Energy spectrum is known to have distinct signatures of activity in continuum models of active matter [20, 21, 24]. We use this idea to present a novel inference framework using deep learning.

We plot the kinetic energy spectrum $E(k)$ in Fig.1(a), and (b) for active model H and active nematics respectively. It can be seen that it is sensitive to the choice of parameters and model. We also find that it changes as a function of time (not shown here). In the following, we use the kinetic energy spectrum to develop our ML model to infer parameters. Usually, in the literature,

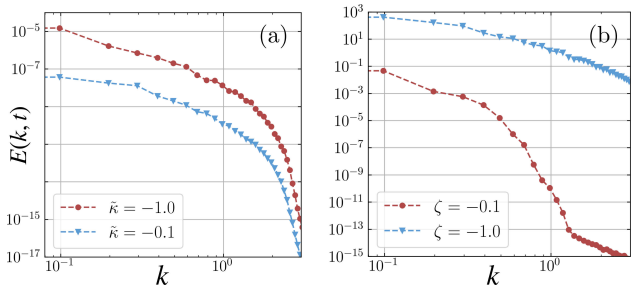

FIG. 3. **Kinetic Energy spectrum**. Panel (a) is the energy Spectrum $E(k, t)$ of active model H for two different values of activity $\tilde{\kappa} = -0.1$ and -1.0, while panel (b) is energy spectrum $E(k, t)$ of active nematics for two different values of activity $\zeta = -0.1$ and -1.0.

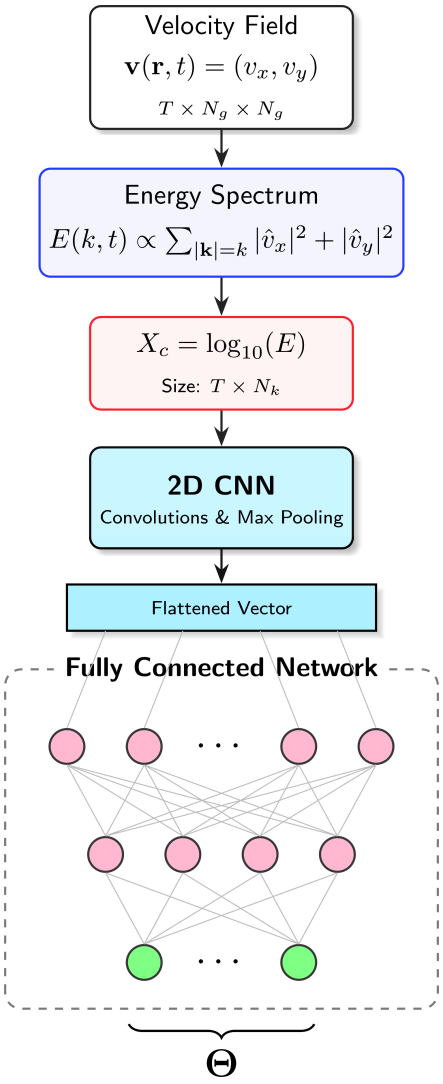

FIG. 4. **Machine Learning Framework**. The velocity field is used to compute the kinetic energy spectrum $E(k,t)$.The spectrum is log-transformed and passed through a 2D CNN, whose output is flattened and mapped through fully connected layers to predict the model parameters Θ: $(\tilde{\kappa}, b, \kappa_p)$ for Active Model H and (ζ, K) for Active Nematics.

the energy spectrum $E(k)$ is average over time. We use the temporal information in the spectrum to infer all the parameters and select between models.

III. MACHINE LEARNING FRAMEWORK

We formulate parameter inference as a supervised regression problem in which the objective is to predict the governing model parameters from the kinetic energy spectrum, $E(k,t)$, computed from flow fields. To this end, we train two convolutional neural networks (CNNs)[28, 29], $\mathcal{N}_{\mathrm{AMH}}$ and $\mathcal{N}_{\mathrm{AN}}$, corresponding to Active Model H and Active Nematics, respectively. Although both networks operate on the same input representation, each is trained to predict the parameter set specific to its underlying continuum model. Specifically, $\mathcal{N}_{\mathrm{AMH}}$ predicts the parameters $(\tilde{\kappa}, b, \kappa_p)$, while $\mathcal{N}_{\mathrm{AN}}$ predicts (ζ, K).

For each trajectory, the kinetic energy spectrum, $E(k,t)$, is evaluated over the late-time statistically stationary regime and represented as a two-dimensional array with wavenumber and time as its axes. To improve numerical stability and compress the large dynamic range of the spectral values, the network input is defined as the logarithmically transformed spectrum, $X_c = \log_{10}(E(k,t) + \varepsilon)$ where ε is a small positive constant introduced to avoid numerical singularities.

A. Network architecture

The transformed spectrum, X_c, is treated as a single-channel image and processed by a convolutional neural network (Fig. 7 of Appendix), exploiting local correlations along both the spectral and temporal axes in a manner analogous to spectrogram-based classification [28, 30]. The network consists of two convolutional blocks followed by a fully connected regression head. The convolutional blocks employ 5×5 and 3×3 kernels, respectively, with LeakyReLU[31] activations and 2×2 max-pooling after each convolution. The extracted features are flattened and mapped to the model parameters through two fully connected hidden layers and a final linear output layer (Fig. 4). The two networks differ only in the dimension of the output layer.

B. Training

Separate training datasets are generated for each continuum model by sampling the physically relevant parameter space while excluding the vicinity of the passive limit, where the activity is too weak to produce distinctive flow patterns. Parameter values are sampled using a combination of a jittered Cartesian grid and random sampling to ensure both broad coverage of the parameter space and dense sampling around representative parameter combinations.

Since the activity parameters, $\tilde{\kappa}$ for Active Model H and ζ for Active Nematics, have fixed signs by convention (corresponding to contractile or extensile activity), the networks are trained to predict the logarithm of their magnitudes. The appropriate sign is then restored after inference according to the prescribed convention. The logarithmic transformed targets are standardized to zero mean and unit variance using a scaler fit on the training set; this scaler is saved and reapplied to invert the predictions back to physical units at the test time.

Networks are implemented in PyTorch [32] and optimized using the AdamW [33] optimizer with a mean-squared-error loss and an 85/15 train-validation split. Model performance is assessed using an independent test

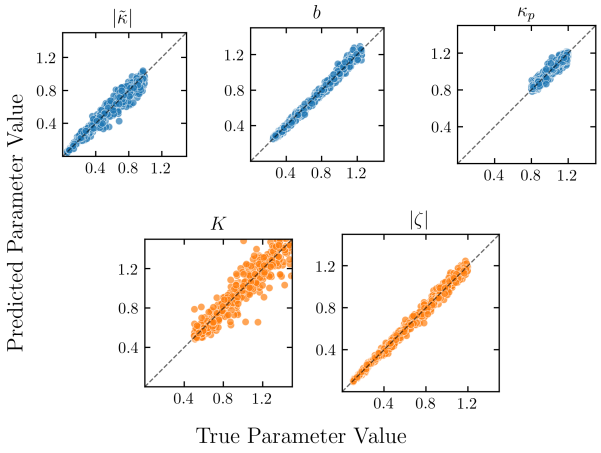

FIG. 5. **Parameter recovery.** Predicted versus true parameter values on the held-out test set, for Active Model H (top row, green: $\tilde{\kappa}$, b, κ_p) and Active Nematics (bottom row, orange: K, ζ). Each point is one test simulation; the dashed line marks perfect recovery ($y = x$).

set comprising simulations not encountered during training. Prediction accuracy is quantified using the mean absolute percentage error (MAPE) between the inferred and true parameter values. The training and validation loss curves, along with the per-parameter percentage error, are shown in Fig. 8 of Appendix A.

C. Parameter recovery

To assess the accuracy of the trained networks, we evaluate parameter recovery on an independent test set of simulations not used during training or validation. Figure 5 shows the predicted versus true values for all inferred parameters: $(\tilde{\kappa}, b, \kappa_p)$ for Active Model H and (ζ, K) for Active Nematics. Predictions for b, K, and ζ lie close to the diagonal across the sampled range. Overall, the tight clustering along $y = x$ demonstrates that the kinetic energy spectrum retains sufficient information to recover the activity parameters directly from flow-field data, without any reference to the underlying order-parameter or nematic director fields. This is consistent with the stable convergence of training and validation loss shown in Fig. 8 of Appendix.

Since the energy spectrum carries distinct signatures of activity in these continuum models, as noted in Sec. II, the map from activity parameters to $E(k, t)$ is expected to be effectively one-to-one over the sampled range. Working with the time-resolved spectrum, rather than its time average, further resolves parameter combinations that converge to similar steady states but differ in fluctuations in time. The absence of deviation in parameter recovery (Fig. 5) and of a validation-loss plateau during training (Fig. 8) is consistent with this map being locally invertible over the sampled parameter range.

Algorithm 1 Model Selection

Require: $v_x(\mathbf{r}, t), v_y(\mathbf{r}, t)$; $\mathcal{N}_{\mathrm{AMH}}, \mathcal{N}_{\mathrm{AN}}$; R
Ensure: $M^*, \theta^*, P(M^*)$
$\mathcal{M} \leftarrow \{\mathrm{AMH}, \mathrm{AN}\}$
Compute $X_c \leftarrow \log_{10}(E(k, t) + \varepsilon)$ from the observed fields
$\theta_{\mathrm{AMH}} = (\tilde{\kappa}, b, \kappa_p) \leftarrow \mathcal{N}_{\mathrm{AMH}}(X_c)$
$\theta_{\mathrm{AN}} = (\zeta, K) \leftarrow \mathcal{N}_{\mathrm{AN}}(X_c)$
Compute the time-averaged spectrum $\log\langle E\rangle_t(k)$ of the observed fields
for $c \in \mathcal{M}$ **do**
  for $r = 1$ to R **do**
    $(\hat{v}_x^{(r)}, \hat{v}_y^{(r)}) \leftarrow \mathcal{S}(\theta_c)$ {new random initial condition}
    Compute $\log\langle \hat{E}^{(r)}\rangle_t$
  end for
  $d_c \leftarrow \dfrac{1}{RN_k} \sum_{r,k} \left[\log\langle E\rangle_t - \log\langle \hat{E}^{(r)}\rangle_t\right]^2$
end for
$\tau \leftarrow \mathrm{median}_c(d_c), \quad P(c) \propto e^{-d_c/\tau}$
$M^* \leftarrow \arg\min_c d_c, \quad \theta^* \leftarrow \theta_{M^*}$
return $M^*, \theta^*, P(M^*)$

IV. MODEL SELECTION

Beyond estimating parameters within a single model, we can also predict which model (AMH or AN) better suits a given velocity field data [34, 35]. A trained network will output parameter values regardless of whether its own model actually describes the observed data, so parameter estimation by itself cannot tell us which model is the right one [36]. To decide between AMH and AN, we go one step further and check each candidate model against the data by re-simulating it [37–40], following the procedure in Algorithm 1 and Fig. 6(a).

Given an observed velocity field, we compute its energy spectrum and pass it through both trained networks, obtaining candidate parameters θ_{AMH} and θ_{AN}. For each candidate, we run new simulations using the predicted parameters, with R independent realizations to account for the randomness in the initial conditions. Because the energy spectrum fluctuates in time even at fixed parameters, we compare models using the time-averaged spectrum, $\log_{10}\langle E(k, t)\rangle_t$, rather than comparing individual snapshots; averaging over time removes fluctuations that are not specific to any one model and retains the steady-state spectral shape that is characteristic of a given parameter set. For each candidate model c, we define a discrepancy score d_c:

$$d_c = \frac{1}{RN_k} \sum_{r,k} \left[\log_{10}\langle E\rangle_t - \log_{10}\langle \hat{E}^{(r)}\rangle_t\right]^2. \tag{12}$$

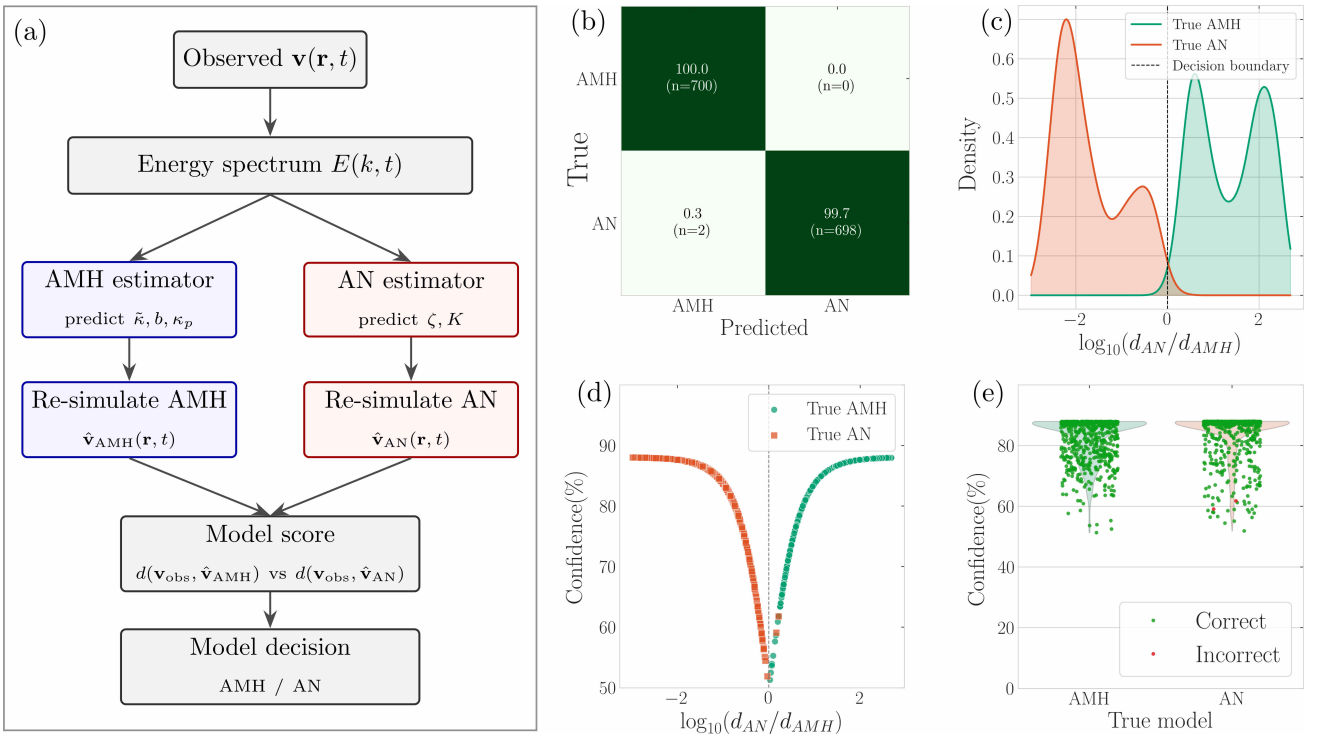

FIG. 6. **Model selection.** (a) Given a flow field data, we first compute the parameters of the model. This is then used to run simulation and compute spectrum. Time average spectrum is compared with the data provided to do model selection. A detailed algorithm is given in Algorithm 1. (b) Confusion matrix for the AMH/AN decision on held-out test cases, reported as per-true-class accuracy with counts. (c) Distribution of the log discrepancy ratio $\log_{10}(d_{\mathrm{AN}}/d_{\mathrm{AMH}})$ for AMH and AN generated test cases, separated by the decision boundary at zero. (d) Assigned confidence $P(M^*)$ as a function of the log discrepancy ratio, for AMH and AN generated test cases. (e) Distribution of confidence $P(M^*)$ by true model, with correctly and incorrectly classified cases shown separately.

In the above, d_c is the the mean squared error, in log space, between the observed $\langle E \rangle_t$ and simulated spectra $\langle \hat{E}^{(r)} \rangle_t$, averaged over the R realizations and over wavenumber bins[38]. The model with the lowest discrepancy is selected as the best match to the data, and its predicted parameters are reported as the inferred activity. We also assign a confidence score [36, 41] to the selected model using a Boltzmann weight, $P(c) \propto \exp(-d_c/\tau)$, where τ is set to the median discrepancy across the candidate models; this gives a normalized probability for each model rather than an arbitrary cutoff on the discrepancy score.

We test this procedure on held-out simulations for which the true generating model is known, running Algorithm 1 on each and comparing the selected model M^* to the ground truth. This tells us how often the resimulation step correctly identifies the generating model, including cases where a network's predicted parameters look reasonable on their own but fail to reproduce the observed spectrum once resimulated.

As shown in Figure 6(b), the algorithm recovers the correct generating model for the large majority of test cases: each model fits its own data substantially better than the other's, so the log discrepancy ratio($\log_{10}(d_{\mathrm{AN}}/d_{\mathrm{AMH}})$) falls almost entirely on one side of zero depending on the true model as shown in Figure 6(c). The assigned confidence reflects this separation directly, falling to its lowest values near the decision boundary and rising toward its maximum as a test case's discrepancy ratio moves further from zero in either direction (Figure 6(d)). The misclassified cases correspond to comparatively low confidence(Figure 6(e)), indicating that the confidence score can serve as an indicator of when a prediction should be treated with caution.

V. SUMMARY AND DISCUSSION

We introduce a machine-learning framework designed to solve the inverse problem of model selection and parameter estimation in continuum models of active matter. While forward modeling traditionally uses material parameters to simulate flow, mapping observable kinematics back to their generative, non-equilibrium forces represents a critical challenge. By treating high-resolution hydrodynamic velocity fields—such as those routinely captured via Particle Image Velocimetry (PIV)—as a diagnostic readout, our framework non-invasively reconstructs internal driving forces and infers underlying activity parameters. Thus, our framework new pathways for

characterizing active matter systems and potential designing ideas for autonomous, smart soft materials. We demonstrate the versatility and robustness of this approach across distinct classes of continuum descriptions, specifically Active Model H and Active Nematics.

The methodology operates across three cascading stages: automated spectral feature conditioning, deep topological pattern encoding via a two-dimensional Convolutional Neural Network (2D CNN), and a rigorous synthetic-ensemble verification loop. A conceptual overview of this pipeline is shown using this algorithm. In this paper, we have considered model inference and selection of AMH and active nematics for two-dimensional systems where the model reduces to a scalar field [24]. Applying the method presented here to three-dimensional systems and models with more complexity suggests an exciting direction for future work.

Machine learning methods have been used to predict the activity from fluid flow in particle-based models [42, 43]. In this paper, we focus on continuum models and chosen two representative model which have activity in the mechanical sector for our inference framework. Thus, the fluid flow retains a high-fidelity signature. Extending our method to cases when the activity is in the diffusive sector [16, 44] suggest a direction for future work. In addition, we have considered a small range for the parameter inference to avoid computational cost. We believe that our model is extendable to larger systems sizes and data in three-dimensions. In Ref.[7] director field data was used for inference which was then used for forecasting future. In our method, we simply use the fluid velocity to obtain the parameters of the model. To find the corresponding dynamics of the order parameter, we need some initial condition which can then be evolved using the parameters. It should be noted that deep learning methodology of this paper is only expected to work for Stokesian fluid-flow data. For more complex scenarios - for example, cases where inertia and/or memory effects in the fluid are important – a very different architectures and strategies of inference and model selection is required.

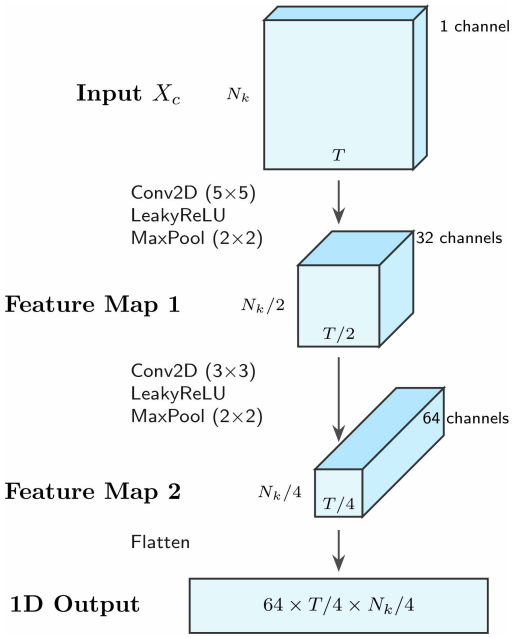

FIG. 7. Processioning of the energy spectrum by the 2D Convolutional Neural Network.

Appendix A: Simulation method

In this section, we explain the numerical methods used to simulate continuum models of active matter with fluid flow. At low Reynolds number, as applicable to active colloidal matter, the fluid flow satisfies the Stokes equation

$$-\boldsymbol{\nabla} p + \eta \nabla^2 \mathbf{v} = -\boldsymbol{f}, \qquad \boldsymbol{\nabla} \cdot \mathbf{v} = 0. \tag{A1}$$

Here, $\boldsymbol{f}$ is the force density in the fluid which is due to activity of the medium. The force density in the fluid is distinct for active model H of section II A and active nematics of section II B.

The forward problem: to determine the flow given the force density. We use Fourier transforms to obtain a solution of the above equations. We define the Fourier transform of a function $\varphi(\boldsymbol{r})$ as

$$\hat{\varphi}(\boldsymbol{k}) = \mathbb{F}\left[\varphi(\boldsymbol{r})\right] = \int \varphi(\boldsymbol{r})\, e^{-i\boldsymbol{k}\cdot\boldsymbol{r}}\, d\boldsymbol{r}, \tag{A2a}$$

$$\varphi(\boldsymbol{r}) = \mathbb{F}^{-1}\left[\hat{\varphi}(\boldsymbol{k})\right] = \frac{1}{(2\pi)^3} \int \hat{\varphi}(\boldsymbol{k})\, e^{i\boldsymbol{k}\cdot\boldsymbol{r}}\, d\boldsymbol{k}. \tag{A2b}$$

We now Fourier transform (A1) to obtain:

$$-i\boldsymbol{k}\hat{p} - \eta k^2 \hat{\boldsymbol{v}} = -\hat{\boldsymbol{f}}, \qquad i\boldsymbol{k}\cdot\hat{\boldsymbol{v}} = 0. \tag{A3}$$

The above equations can then be used to obtain the Fourier transform of the pressure field (note that all isotropic terms have been absorbed in the pressure, which is then used to ensure the incompressibility condition): $\hat{p} = -i\boldsymbol{k}\cdot\hat{\boldsymbol{f}}/k^2$.. The above expression of the pressure is then used in (A3) to obtain the solution of the fluid flow, with built-in incompressibility, given as

$$\hat{\boldsymbol{v}} = \hat{\mathbf{G}}(\boldsymbol{k})\cdot\hat{\boldsymbol{f}}, \qquad \hat{\mathbf{G}}(\boldsymbol{k}) = \frac{1}{\eta}\left(\frac{\boldsymbol{I}}{k^2} - \frac{\boldsymbol{k}\boldsymbol{k}}{k^4}\right). \tag{A4}$$

Here $\hat{\mathbf{G}}(\boldsymbol{k})$ is the Fourier transform of the Oseen tensor $\mathbf{G}(\boldsymbol{r})$ [45]. Using the above solution, the simulations are performed using the pseudo-spectral method [46, 47]. The solution for the fluid flow and order parameter is numerically implemented using standard fast Fourier transforms (FFTs). Thus, periodic boundary conditions are automatically ensured in the system.

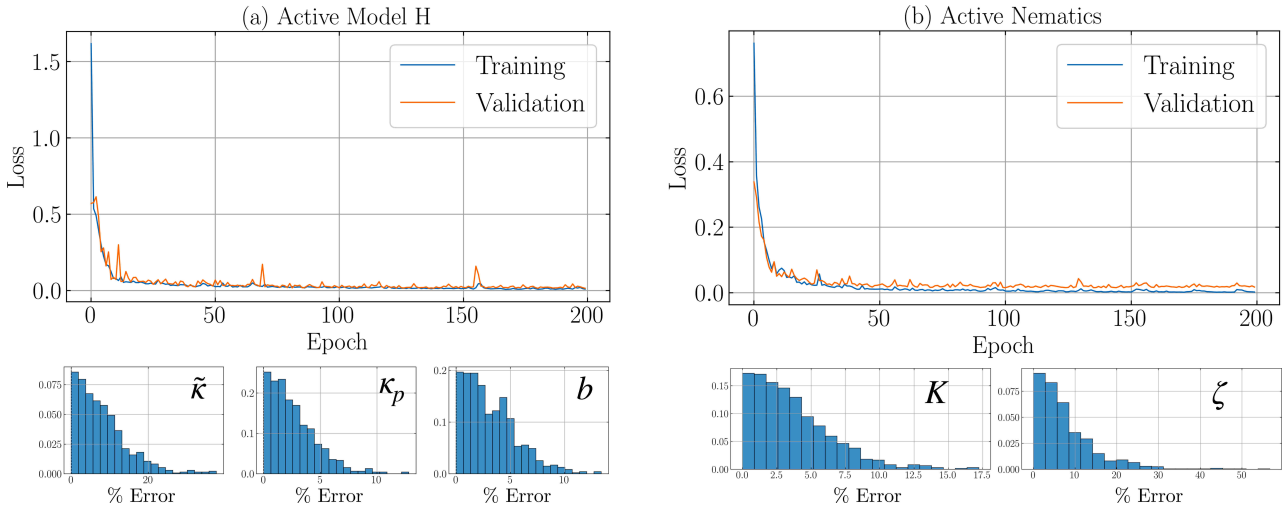

FIG. 8. (a) Convergence plot of Active Model H: Training and Validation loss versus epoch, $\tilde{\kappa}$ prediction percentage error, κ_p prediction percentage error, and b prediction percentage error. (b) Convergence plot of Active nematics model: Training and Validation loss versus epoch, K prediction percentage error, and ζ prediction percentage error.

Appendix B: ML framework

1. The 2D Convolutional Neural Network

The figure 7 shows how the 2D Convolutional Neural Network processes the energy spectrum. The network treats the 2D spectrum like an image, passing it through two sequential processing blocks. Each block uses a convolutional layer, followed by a pooling layer that reduces the spatial resolution. s the feature maps become progressively smaller in the temporal and spectral dimensions, the number of channels increases, allowing the network to encode more abstract and discriminative patterns. The final feature map is reshaped into a one-dimensional vector, which serves as the input to subsequent stages of the model.

2. Convergence plot

The convergence of the ML framework is shown in Fig.8. It can be seen that that training loss and validation loss decreases over epochs. Thus, it indicates that the model is learning well without overfitting to the data.

[1] M. E. Cates and F. C. MacKintosh, Active soft matter, Soft Matter **7**, 3050 (2011).
[2] S. Ramaswamy, The Mechanics and Statistics of Active Matter, Annu. Rev. Condens. Mat. Phys. **1**, 323 (2010).
[3] M. C. Marchetti, J. F. Joanny, S. Ramaswamy, T. B. Liverpool, J. Prost, M. Rao, and R. A. Simha, Hydrodynamics of soft active matter, Rev. Mod. Phys. **85**, 1143 (2013).
[4] M. te Vrugt, B. Liebchen, and M. E. Cates, Colloquium: What do we mean by 'active matter'?, Reviews of Modern Physics **98**, 031001 (2026).
[5] M. E. Cates and C. Nardini, Active phase separation: new phenomenology from non-equilibrium physics, Reports on Progress in Physics **88**, 056601 (2025).
[6] R. Alert, J. Casademunt, and J.-F. Joanny, Active turbulence, Annual Review of Condensed Matter Physics **13**, 143 (2022).
[7] J. Colen, M. Han, R. Zhang, S. A. Redford, L. M. Lemma, L. Morgan, P. V. Ruijgrok, R. Adkins, Z. Bryant, Z. Dogic, *et al.*, Machine learning active-nematic hydrodynamics, Proceedings of the National Academy of Sciences **118**, e2016708118 (2021).
[8] C. Joshi, S. Ray, L. M. Lemma, M. Varghese, G. Sharp, Z. Dogic, A. Baskaran, and M. F. Hagan, Data-driven discovery of active nematic hydrodynamics, Phys. Rev. Lett. **129**, 258001 (2022).
[9] Z. Zhou, C. Joshi, R. Liu, M. M. Norton, L. Lemma, Z. Dogic, M. F. Hagan, S. Fraden, and P. Hong, Machine learning forecasting of active nematics, Soft Matter **17**, 738 (2021), https://pubs.rsc.org/sm/article-pdf/17/3/738/7579440/d0sm01316a.pdf.
[10] J. Zaplotnik, J. Pišljar, M. Škarabot, and M. Ravnik, Neural networks determination of material elastic constants and structures in nematic complex fluids, Scientific reports **13**, 6028 (2023).
[11] A. Piven, D. Darmoroz, E. Skorb, and T. Orlova, Machine learning methods for liquid crystal research: phases, textures, defects and physical properties, Soft Matter **20**, 1380 (2024), https://pubs.rsc.org/sm/article-pdf/20/7/1380/9444082/d3sm01634j.pdf.
[12] A. Frishman and K. Keren, Learning active nematics one step at a time, Proceedings of the National Academy of

Sciences **118**, e2102169118 (2021).
[13] M. Golden, R. O. Grigoriev, J. Nambisan, and A. Fernandez-Nieves, Physically informed data-driven modeling of active nematics, Science Advances **9**, eabq6120 (2023).
[14] A. Tiribocchi, R. Wittkowski, D. Marenduzzo, and M. E. Cates, Active model H: scalar active matter in a momentum-conserving fluid, Phys. Rev. Lett. **115**, 188302 (2015).
[15] R. Singh and M. E. Cates, Hydrodynamically interrupted droplet growth in scalar active matter, Phys. Rev. Lett. **123**, 148005 (2019).
[16] M. E. Cates, Active field theories, arXiv preprint arXiv:1904.01330 (2019).
[17] S. Shankar, A. Souslov, M. J. Bowick, M. C. Marchetti, and V. Vitelli, Topological active matter, Nature Reviews Physics **4**, 380 (2022).
[18] S. Ramaswamy, Active matter, J. Stat. Mech. **2017**, 054002 (2017).
[19] P. C. Hohenberg and B. I. Halperin, Theory of dynamic critical phenomena, Rev. of Mod. Phys. **49**, 435 (1977).
[20] N. B. Padhan and R. Pandit, The cahn–hilliard–navier–stokes framework for multiphase fluid flows: laminar, turbulent and active, Journal of Fluid Mechanics **1010**, P1 (2025).
[21] B. N. Radhakrishnan, F. Serafin, T. L. Schmidt, and É. Fodor, Irreversibility in scalar active turbulence: the role of topological defects, New Journal of Physics **28**, 034601 (2026).
[22] L. D. Landau and E. M. Lifshitz, *Fluid mechanics*, Vol. 6 (Pergamon Press, New York, 1959).
[23] A. Doostmohammadi, J. Ignés-Mullol, J. M. Yeomans, and F. Sagués, Active nematics, Nature communications **9**, 3246 (2018).
[24] R. Alert, J.-F. Joanny, and J. Casademunt, Universal scaling of active nematic turbulence, Nature Physics **16**, 682 (2020).
[25] S. Mukherjee, R. K. Singh, M. James, and S. S. Ray, Intermittency, fluctuations and maximal chaos in an emergent universal state of active turbulence, Nature Physics **19**, 891 (2023).
[26] R. A. Simha and S. Ramaswamy, Hydrodynamic Fluctuations and Instabilities in Ordered Suspensions of Self-Propelled Particles, Phys. Rev. Lett. **89**, 058101 (2002).
[27] F. Jülicher, S. W. Grill, and G. Salbreux, Hydrodynamic theory of active matter, Reports on Progress in Physics **81**, 076601 (2018).
[28] Y. Lecun, L. Bottou, Y. Bengio, and P. Haffner, Gradient-based learning applied to document recognition, Proceedings of the IEEE **86**, 2278 (1998).
[29] I. Goodfellow, Y. Bengio, and A. Courville, *Deep Learning* (MIT Press, 2016) `http://www.deeplearningbook.org`.
[30] S. Hershey, S. Chaudhuri, D. P. W. Ellis, J. F. Gemmeke, A. Jansen, C. Moore, M. Plakal, D. Platt, R. A. Saurous, B. Seybold, M. Slaney, R. Weiss, and K. Wilson, Cnn architectures for large-scale audio classification, in *International Conference on Acoustics, Speech and Signal Processing (ICASSP)* (2017).
[31] A. L. "Maas, A. Y. "Hannun, and A. Y. "Ng, Rectifier nonlinearities improve neural network acoustic models (2013).
[32] A. Paszke, S. Gross, F. Massa, A. Lerer, J. Bradbury, G. Chanan, T. Killeen, Z. Lin, N. Gimelshein, L. Antiga, A. Desmaison, A. Köpf, E. Yang, Z. DeVito, M. Raison, A. Tejani, S. Chilamkurthy, B. Steiner, L. Fang, J. Bai, and S. Chintala, Pytorch: an imperative style, high-performance deep learning library, in *Proceedings of the 33rd International Conference on Neural Information Processing Systems* (Curran Associates Inc., Red Hook, NY, USA, 2019).
[33] I. Loshchilov and F. Hutter, Decoupled weight decay regularization, in *International Conference on Learning Representations* (2019).
[34] D. J. MacKay, *Information theory, inference and learning algorithms* (Cambridge university press, 2003).
[35] D. Sivia and J. Skilling, *Data analysis: a Bayesian tutorial* (OUP Oxford, 2006).
[36] E. T. Jaynes, *Probability theory: The logic of science* (Cambridge university press, 2003).
[37] K. Cranmer, J. Brehmer, and G. Louppe, The frontier of simulation-based inference, Proceedings of the National Academy of Sciences **117**, 30055 (2020), https://www.pnas.org/doi/pdf/10.1073/pnas.1912789117.
[38] T. Toni, D. Welch, N. Strelkowa, A. Ipsen, and M. P. Stumpf, Approximate bayesian computation scheme for parameter inference and model selection in dynamical systems, Journal of The Royal Society Interface **6**, 187 (2008), https://royalsocietypublishing.org/rsif/article-pdf/6/31/187/489132/rsif.2008.0172.pdf.
[39] R. Singh, D. Ghosh, and R. Adhikari, Fast Bayesian inference of the multivariate ornstein-uhlenbeck process, Phys. Rev. E **98**, 012136 (2018).
[40] S. Sisson, Y. Fan, and M. Beaumont, *Handbook of Approximate Bayesian Computation*, Chapman and Hall/CRC Handbooks of Modern Statistical Methods Series (CRC Press, Taylor and Francis Group, 2019).
[41] R. E. Kass and A. E. Raftery, Bayes factors, Journal of the American Statistical Association **90**, 773 (1995).
[42] A. Mohapatra, A. Kumar, M. Deb, S. Dhomkar, and R. Singh, Inferring activity from the flow field around active colloidal particles using deep learning, Journal of Fluid Mechanics **1018**, R1 (2025).
[43] P. Bayati and S. A. Mallory, Inferring surface slip in active colloids from flow fields using physics-informed neural networks, arXiv preprint arXiv:2511.22723 (2025).
[44] E. Tjhung, C. Nardini, and M. E. Cates, Cluster phases and bubbly phase separation in active fluids: Reversal of the ostwald process, Phys. Rev. X **8**, 031080 (2018).
[45] C. Pozrikidis, *Boundary Integral and Singularity Methods for Linearized Viscous Flow* (Cambridge U.P., 1992).
[46] J. P. Boyd, *Chebyshev and Fourier spectral methods* (Courier Corporation, 2001).
[47] J. N. Kutz, *Data-driven modeling & scientific computation: methods for complex systems & big data* (Oxford University Press, 2026).